

Article

Electrocatalytic CO₂ Reduction and H₂ Evolution by a Copper (II) Complex with Redox-Active Ligand

Jingjing Li ¹, Shifu Zhang ¹, Jinmiao Wang ¹, Xiaomeng Yin ¹, Zhenxing Han ¹, Guobo Chen ¹, Dongmei Zhang ¹ and Mei Wang ^{1,2,*}

¹ Key Laboratory of Marine Chemistry Theory and Technology, Ministry of Education, College of Chemistry and Chemical Engineering, Ocean University of China, Qingdao 266100, China; lj11@stu.ouc.edu.cn (J.L.); zhangshifu@stu.ouc.edu.cn (S.Z.); wangjinmiao@stu.ouc.edu.cn (J.W.); yinxiaomeng@stu.ouc.edu.cn (X.Y.); hanzhenxing66@163.com (Z.H.); chenguobo@ouc.edu.cn (G.C.); zdmei@ouc.edu.cn (D.Z.)

² Institute for New Energy Materials & Low Carbon Technologies, School of Materials Science and Engineering, Tianjin University of Technology, Tianjin 300384, China

* Correspondence: meiwang@ouc.edu.cn

Abstract: The process of electrocatalytic CO₂ reduction and H₂ evolution from water, regarding renewable energy, has become one of the global solutions to problems related to energy consumption and environmental degradation. In order to promote the electrocatalytic reactivity, the study of the role of ligands in catalysis has attracted more and more attention. Herein, we have developed a copper (II) complex with redox-active ligand [Cu(L¹)₂NO₃]₂NO₃ (**1**, L¹ = 2-(6-methoxypyridin-2-yl)-6-nitro-1h-benzo [D] imidazole). X-ray crystallography reveals that the Cu ion in cation of complex **1** is coordinated by two redox ligands L¹ and one labile nitrate ligand, which could assist the metal center for catalysis. The longer Cu-O bond between the metal center and the labile nitrate ligand would break to provide an open coordination site for the binding of the substrate during the catalytic process. The electrocatalytic investigation combined with DFT calculations demonstrate that the copper (II) complex could homogeneously catalyze CO₂ reduction towards CO and H₂ evolution, and this could occur with great performance due to the cooperative effect between the central Cu (II) ion and the redox-active ligand L¹. Further, we discovered that the added proton source H₂O and TsOH·H₂O (p-Toluenesulfonic acid) could greatly enhance its electrocatalytic activity for CO₂ reduction and H₂ evolution, respectively.

Keywords: copper (II) complex; redox-active ligand; electrocatalysis; CO₂ reduction; H₂ evolution



Citation: Li, J.; Zhang, S.; Wang, J.; Yin, X.; Han, Z.; Chen, G.; Zhang, D.; Wang, M. Electrocatalytic CO₂ Reduction and H₂ Evolution by a Copper (II) Complex with Redox-Active Ligand. *Molecules* **2022**, *27*, 1399. <https://doi.org/10.3390/molecules27041399>

Academic Editor: Michal Szostak

Received: 31 December 2021

Accepted: 14 February 2022

Published: 18 February 2022

Publisher's Note: MDPI stays neutral with regard to jurisdictional claims in published maps and institutional affiliations.



Copyright: © 2022 by the authors. Licensee MDPI, Basel, Switzerland. This article is an open access article distributed under the terms and conditions of the Creative Commons Attribution (CC BY) license (<https://creativecommons.org/licenses/by/4.0/>).

1. Introduction

The enormous global consumption of fossil fuel leads to critical environmental, energy, and climate issues [1]. Several promising strategies have been developed to resolve the above issues. Firstly, applying renewable electricity to drive CO₂ into high-value fuels such as carbon monoxide (CO), formic acid (HCOOH), methanol (CH₃OH), and methane (CH₄), etc., has been considered a sustainable route to alleviate energy shortages and global warming [2]. Secondly, as a green energy and high energy carrier, hydrogen (H₂) is a great candidate to replace fossil fuels in the near future [3]. Therefore, catalytic hydrogen evolution reaction (HER), with high efficiency and low cost, has become a hot research area [4]. Thirdly, due to the similar reduction potentials, HER is the main competing reaction during electrocatalytic CO₂ reduction reaction (CO₂RR), which is a crucial problem to be solved for CO₂RR [5]. Nevertheless, the competition reactions of HER and CO₂RR can be rationally used in exploring efficient ways to produce syngas, the gaseous mixture of CO and H₂, which are very useful in producing fuels such as alcohols, hydrocarbon, dimethyl ether, and more fuels through the industrial Fischer–Tropsch process, etc. [6].

In recent years, the uses of low-cost non-precious transition metal complexes as catalysts have aroused the interest of researchers. Among these non-precious metal complexes,

due to the special electron structure of copper, copper complexes have been confirmed to be effective electrocatalysts in various reactions. In 2021, Lan et al. reported a copper (I) based complex with excellent electrocatalytic selectivity for CO₂-to-CH₄ reduction, which occurs because of the chalcophile interactions in crystalline catalysts [7]. Mitsopoulou and coworkers investigated the electrocatalytic activity for hydrogen evolution of a Cu (I) diimine complex, and they found that the coordinated nitrogen atoms play an important role, while Yang's group developed a copper (0) enriched material to tune the syngas production with great electrochemical activity [8,9].

In order to promote the electrocatalytic reactivity, the study of the role of ligands in catalysis has attracted more and more attention [10]. Redox-active ligands, e.g. non-innocent ligands, have been affirmed to be a multifunctional tool for improving electrocatalysis both dynamically and thermodynamically, because they can act as an electron reservoir to accept or donate electrons, regulating the electronic properties of the central metal ions, etc. [11–13]. Those extraordinary features enable the redox active ligands to facilitate various catalysis of the transition metal complexes with high reactivity. Jurss' group reported a cobalt (II) complex with bipyridyl-NHC ligand, showing high selectivity for electrocatalytic CO₂ reduction to CO, occurring due to the redox-active synergy effect between the cobalt center and redox-active ligands [14]. Our group also explored the crucial effect of the redox-active ligand bis(imino)pyridine (PDI) on the electrocatalytic activity for CO₂ reduction [15]. Hess and co-workers investigated the electrocatalytic H₂ evolution by a Co (II) complex bearing macrocycle ligand, and they found that the redox-active ligand could modulate the energy and activity of HER [16]. Marinescu's group prepared a cobalt (II) complex with thiolate ligand, and they found that protonation of the redox non-innocent ligand could influence the electrocatalytic reactivity for syngas generation [17]. Imidazole and its derivatives, as forms of redox-active ligands with various structures and rich electrons, have been proven to assist and even stabilize the metal centers in electrocatalytic reactions [18–20].

Regarding the aforementioned reasons, we have synthesized an imidazole derivative redox-active ligand **L**¹, 2-(6-methoxy-pyridin-2-yl)-6-nitro-1*H*-benzo [D] imidazole, and obtained a copper (II) complex [Cu(**L**¹)₂NO₃]NO₃ (**1**) in which the central Cu (II) ion is coordinated by this ligand. The cation of complex **1** is coordinated by two redox ligands **L**¹ and one labile nitrate ligand. The systematic electrocatalysis investigation of complex **1** reveals that it can homogeneously electrocatalyze CO₂ reduction and H₂ evolution, and this occurs with great performance owing to the cooperative effect between the redox-active ligand **L**¹ and the metal center Cu (II). The added proton source, H₂O, could highly enhance its electrocatalytic efficiency for CO₂ reduction to CO. Meanwhile, in the process of catalytic CO₂ reduction to CO, there is an inevitable competition reaction of hydrogen generation, which is a promising process for the synthesis of syngas, with the mixture of CO and H₂. Therefore, we also investigated its catalytic reactivity for H₂ evolution, and we found that the added proton source TsOH·H₂O could highly enhance its electrocatalytic activity for H₂ evolution.

2. Results and Discussion

2.1. The Nature and Character of the Complex

X-ray crystallography demonstrates that complex **1** belongs to monoclinic crystal and the space group is *C12/c1* system (Table S1, Supplementary Materials). The cation of complex **1** is surrounded by two redox-active ligands **L**¹ and one labile nitrate ligand. According to the bond valence sum calculations, the oxidation state of the copper atom in the complex is +2 [21]. As presented in Figure S17 (Supplementary Materials), the magnetic moment (μ_{eff}) of complex **1** at room temperature is around 1.80 μB , and, in addition, the ligand **L**¹ and the copper ion did not undergo reduction during the synthesis procedure, which confirms that the copper ion should be in +2 oxidation state. Furthermore, according to the bond valence sum calculations, the copper atom in the complex is in +2 oxidation state [21]. The metal center Cu^{II} in the complex is coordinated with four N atoms from

the ligand L^1 and two O atoms from the nitrate ligand, forming a twisted tetravacant octahedral construction, as illustrated in Figure 1 and Table S9 (according to the analysis of SHAPE). The coordination geometry of complex **1** can be classified as a distorted four vacancy octahedron (vOC-2, 3C2v). Due to the special d^9 electronic configuration of the metal center Cu^{II} ion, it is witnessed that the Jahn-Teller effect and Bailar distortions of the octahedron and Cu1-N6 and Cu1-O4 bonds are distorted almost on the same axis [22–24]. Meanwhile, the longer Cu-O bond between the metal center and the labile nitrate ligand would break to provide an open coordination site for the binding of the substrate during the catalytic process [25,26].

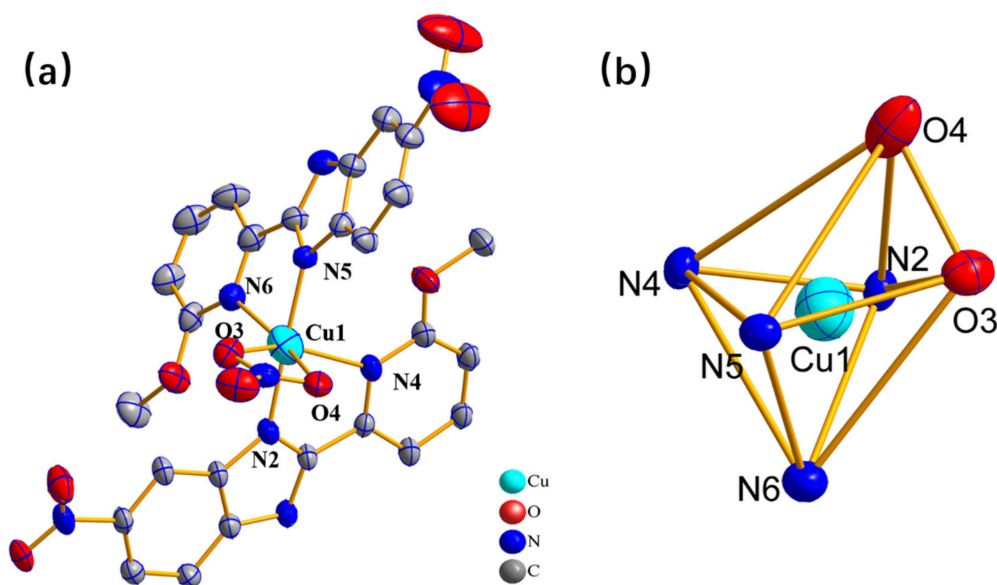


Figure 1. (a) The crystal structure of the complex **1**. (b) The spatial configuration of the complex **1**, all are 50% probability ellipsoids. Color codes: green, Cu; red, O; blue, N; gray, C; and hydrogen atoms are omitted for clear visibility.

2.2. Electrochemistry under Atmosphere of 1 atm Ar

The cyclic voltammograms (CVs) of complex **1**, obtained at different scanning rates ($100\text{--}500\text{ mV s}^{-1}$), in the electrolyte solution of $0.1\text{ M } n\text{Bu}_4\text{NPF}_6/\text{CH}_3\text{CN}$ in the argon (Ar) atmosphere, are displayed in Figure 2. When scanning towards cathode potentials, it can be observed that the complex has three irreversible reduction peaks at the potentials of -1.38 V , -1.97 V and -2.59 V vs. NHE (all the potentials are versus NHE) (Figure 2). Based on the DFT calculation, the LUMOs (lowest unoccupied molecular orbital) of complex **1** are mainly localized on the redox-active ligand L^1 . (Figure 3, the frontier molecular orbital surfaces of **1** are depicted in Figures S2 and S3, Table S4, Supplementary Materials). We have performed the Cyclic voltammetry under Ar atmosphere for the ligand L^1 (Figure S5, Supplementary Materials), which displays two reduction peaks at the potential of -0.48 V and -0.93 V . By comparing the reduction potentials of the ligand L^1 , the first two reduction peaks of complex **1** may be attributed to the reduction of the two redox active ligands L^1 and the according two radical anions $[L^{1\bullet}]$. Meanwhile, the last reduction wave can be ascribed to the Cu^{II}/Cu^I couple. In addition, as shown in Figure 2b, the cathode current peaks (ip) at different scanning rates have a good linear correlation with the square root of the scanning rates, which proves that the electrode process is mainly a diffusion control process. We have listed all the data in these figures in the corresponding tables, as shown in Tables S5–S8 (Supplementary Materials).

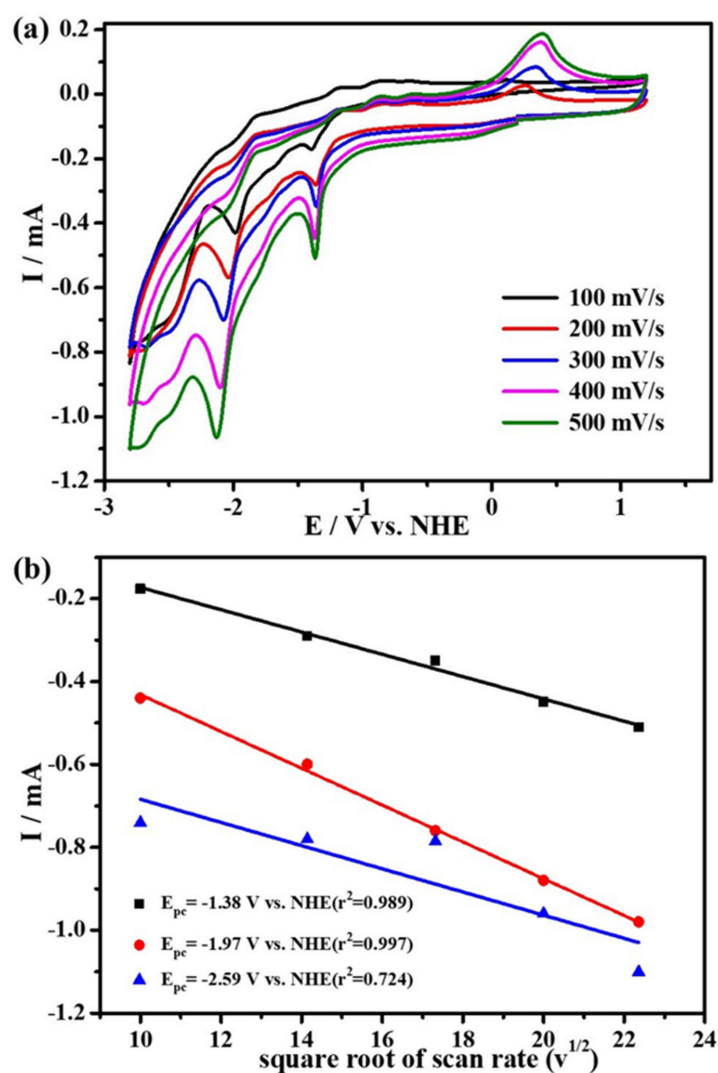


Figure 2. (a) cyclic voltammetry of 2 mM complex 1 under 1 atm Ar with 0.1 M $n\text{Bu}_4\text{NPF}_6$ as supporting electrolyte at scan rates range from 100 to 500 mV s^{-1} ; and (b) the linear relationships between the peak cathodic currents and the square root of scan rates.

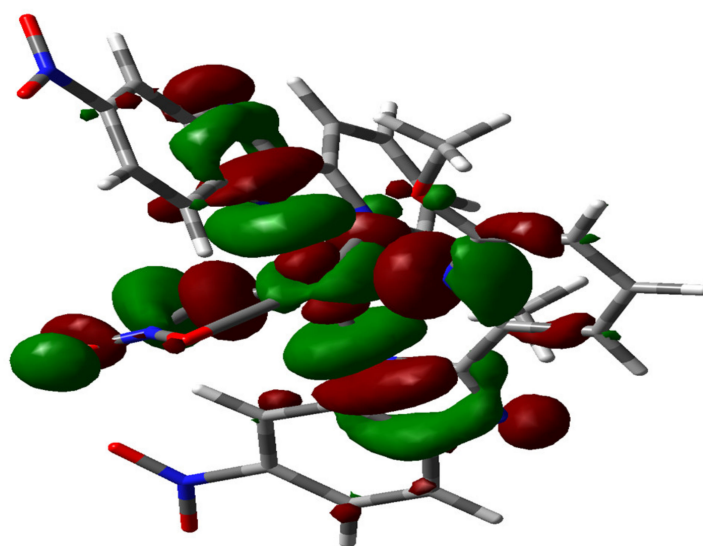


Figure 3. LUMO of complex 1 (iso value = 0.02).

2.3. Electrochemistry in the Presence of CO₂

The electrocatalytic performance for CO₂ reduction of compound **1** was investigated under saturated CO₂ atmosphere with 0.1 M ⁿBu₄NPF₆ as the supporting electrolyte in MeCN solution. The cyclic voltammetry curves at −1.15 V under 1 atm CO₂ are subtracted from the base line. We mainly studied the comparison of catalytic current of complex **1** at 100 mV s^{−1} in CO₂ and Ar at −1.15 V, as shown in Figure S10 (Supplementary Materials). By carrying out cyclic voltammetry experiments on glassy carbon (GC) electrodes, we found that the CV plot in CO₂ displays an enhanced irreversible reduction wave at −1.15 V compared with that in Ar atmosphere at the same scanning rate, while it also repeats very well at different scanning rates without new oxidation or reduction peaks emerging, as illustrated in Figure 4. In addition, we used FTO as the working electrode to perform controlled potential electrolysis of 2mM complex **1** in order to characterize the stability of our catalyst and determine the Faraday efficiency according to the literature reported before [27], and we detected CO based on GC (Gas Chromatography) analysis. All these results indicate that compound **1** can electrocatalytically reduce CO₂ to CO with great stability. Additionally, as illustrated in Figure 5, in order to explore the electrocatalytic activity for CO₂-to-CO of complex **1** in the presence of proton donor, different concentrations of H₂O were added to the CO₂ saturated MeCN solution as the proton source for the CV experiments under the same condition. We have observed that, by the addition of H₂O, the reductive peak current density increases, which suggests that the addition of proton source can promote its catalytic reactivity for CO₂ reduction, and the catalytic reaction should be a PCET process [25]. Furthermore, Figure 6 and Table S8 (Supplementary Materials) show the concentrations of complex **1** as exhibiting linear relationship with the catalytic currents at the catalytic potential of −1.15 V, which suggests that the catalytic CO₂-to-CO conversion is the first-order reaction.

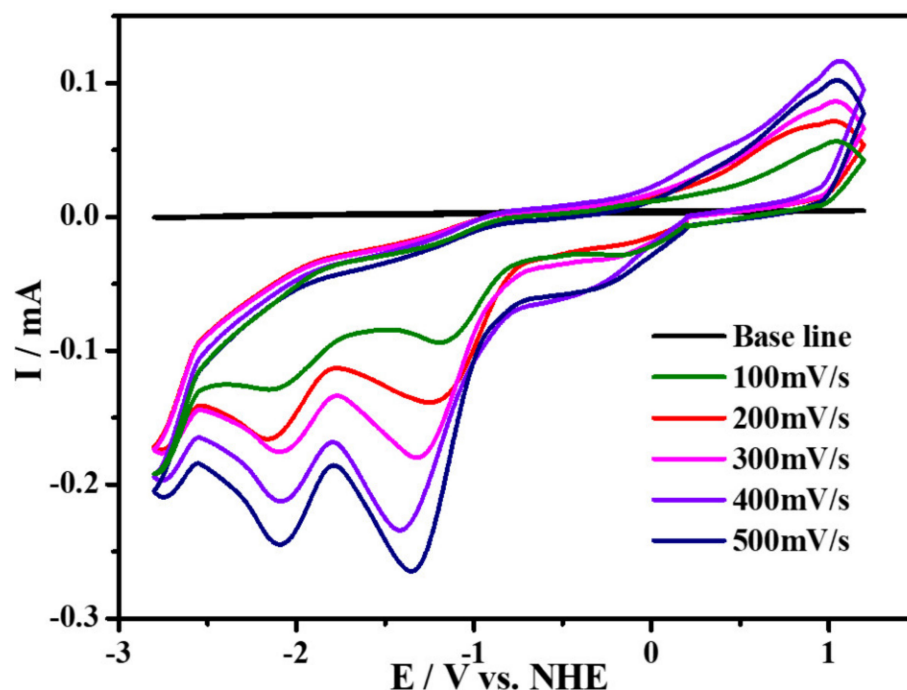


Figure 4. Cyclic voltammograms of 2 mM complex under 1 atm CO₂ at scan rates range from 100 to 500 mV s^{−1} (all the plots are subtracted from the baseline).

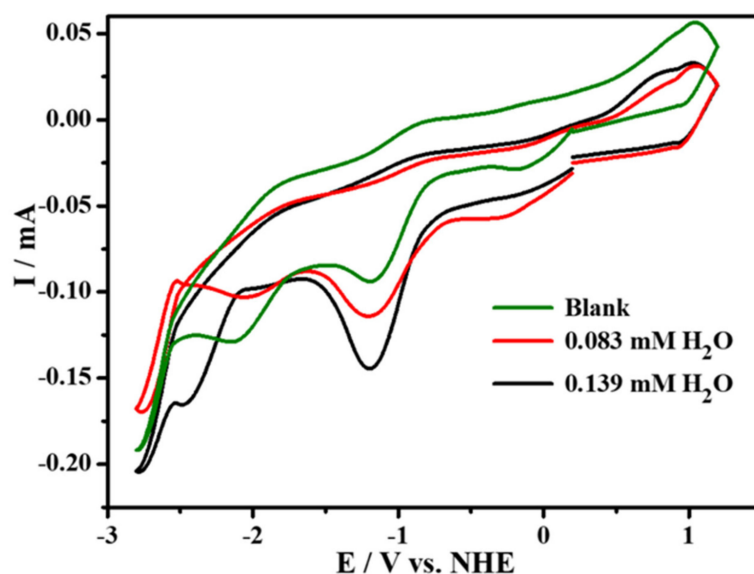


Figure 5. Cyclic voltammograms of the complex 1 containing the H₂O system at different concentrations in the CO₂ atmosphere. Scan rate: 100 mV s⁻¹. Working electrode: glassy carbon. Counter-electrode: Pt wire. Reference electrode: Ag/AgCl.

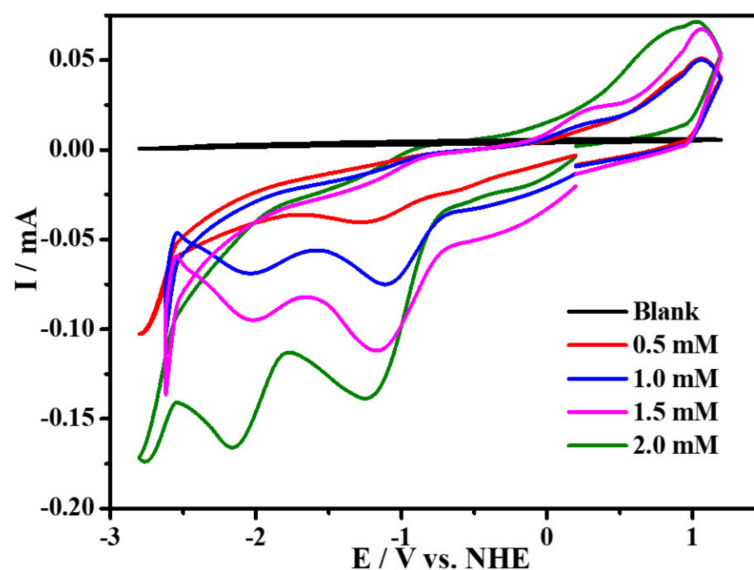


Figure 6. Cyclic voltammograms of the complex 1 at different concentrations in the CO₂ atmosphere. Scan rate: 100 mV s⁻¹.

The turnaround frequency (TOF) of the electrocatalytic CO₂ of complex 1 can be determined by the Equation (1) below:

$$\text{TOF} = \frac{Fvn_p^3}{RT} \left(\frac{0.4463}{n_{\text{cat}}} \right)^2 \left(\frac{i_{\text{cat}}}{i_p} \right)^2 \quad (1)$$

F is the Faraday constant (96,485 C·mol⁻¹), v is the scanning rate used (0.1 V s⁻¹), n_p is the number of electrons involved in the non-catalytic oxidation reduction reaction ($n_p = 1$), and R is the gas constant (8.314 J·K⁻¹·mol⁻¹), T is temperature (293.15 K), n_{cat} is the number of electrons involved in the catalytic reaction ($n_{\text{cat}} = 2$ indicates the reduction of CO₂ to carbon monoxide), i_p and i_{cat} are identified as peak currents under Ar and CO₂, respectively. By Equation (1), TOF is calculated as 0.65 s⁻¹ at the potential of -1.15 V vs.

NHE ($i_{\text{cat}}/i_{\text{p}} = 1.82$), which is comparable with those reported copper based homogeneous catalysts [28–31].

In order to further explore the electrocatalytic ability of this complex for CO_2 reduction, a series of CPE experiments were recorded in CO_2 saturated CH_3CN solution, with the addition of distilled water as the proton source. As shown in Figure S7 (Supplementary Materials), by the red line, during 4000 s electrolysis, the current density can reach $\sim -1.5 \text{ mA cm}^{-2}$ at the potential of -1.15 V vs. NHE in presence of 2 mM complex 1 and 0.139 mM water; the mixed-gas CO and H_2 are detected, which reveals that complex 1 is a potential catalyst for producing syngas [27–29]. As demonstrated in Figure S9 (Supplementary Materials), according to the GC analysis, the calculated Faraday efficiency (FE) of CO evolution is nearly 10% and is about 90%. Furthermore, the current density is very small at the potential of -1.15 V vs. NHE without complex 1 (the black line), and no CO or H_2 is detected, indicating that no catalysis occurs. Additionally, we also examined the solution after electrolysis by MS analysis, but we did not observe HCOOH or CH_3OH . Moreover, the almost linear curve of CPE indicates that catalyst 1 can remain stable in solution throughout the catalytic process. Meanwhile, as shown in Figure S7 (Supplementary Materials), the rinse test was also conducted on the FTO glass electrode after electrocatalysis, displaying nearly no current density, similar with that of the blank test before the catalysis, which assures that complex 1 is a stable homogeneous catalyst. Additionally, we have carried out DLS (dynamic light scattering) of complex 1 before and after 4000 s electrolysis in MeCN solution (Figure S15b, Supplementary Materials), which reveals that the particle distributions are in the range of the molecular hydrodynamic diameter of the cluster, indicating that there are no nanoparticles formed during electrolysis. In addition, Figure S8 illustrates the in-situ UV–vis spectroelectrochemistry of complex 1, conducted during 4000 s CPE, which shows that there is close to no difference in the spectrum, proving the high stability of catalyst 1 during electrolysis. During the reduction process, the longer Cu–O bond between the metal center and the labile nitrate ligand could break to provide an open coordination site for the binding of the substrate CO_2 to produce the possible intermediate Cu-COO^* [23,24]. More importantly, via two reduction steps, the two redox-active ligands are both reduced to radical anions $[\text{L}^{\bullet}]$, which could assist the metal center to cooperatively catalyze CO_2 reduction [10].

2.4. Electrocatalytic Property for Hydrogen Evolution

The electrocatalytic property for hydrogen evolution (HER) of complex 1 was also investigated in CH_3CN (0.1 M $n\text{Bu}_4\text{NPF}_6$) electrolyte solution with the addition of *p*-Toluenesulfonic acid ($\text{TsOH}\cdot\text{H}_2\text{O}$) as the proton source. As depicted in Figure 7, compared with the CV plot without addition of the proton source, it can be found that, with the increasing amounts of *p*-Toluenesulfonic acid added in the solution, the peak currents at the potential of -1.97 V are greatly enhanced. Meanwhile, we detected amounts of H_2 by GC analysis, by CPE experiments, at this potential. These results prove that the reduction reaction of H^+ can occur in the presence of complex 1 at the presence of *p*-Toluenesulfonic acid. In order to further study the electrocatalytic ability of complex 1 for hydrogen evolution, a series of CPE experiments were carried out for 4000 s in CH_3CN with and without *p*-Toluenesulfonic acid at different potentials using FTO working electrode, which suggest that, with 0.58 mM of *p*-Toluenesulfonic acid at the potential of -1.97 V , the current density can reach $\sim 5 \text{ mA cm}^{-2}$, as illustrated in Figure 8. Furthermore, in order to prove that H_2 is not produced by $\text{TsOH}\cdot\text{H}_2\text{O}$, the comparative CV experiment, containing solely $\text{TsOH}\cdot\text{H}_2\text{O}$ in CH_3CN solution without complex 1, is carried out, indicating that there are no reduction waves around -1.97 V (Figures S13 and S14, Supplementary Materials). Beyond this finding, in the absence of complex 1, the current density at -1.97 V is negligible, which suggests that no catalytic reaction occurs without complex 1. According to Equation (1), Equations (S1) and (S2), the calculated TOF of H_2 evolution is 0.33 s^{-1} , and FE is shown in Figure S16 (Supplementary Materials), which is comparable with those reported copper based homogeneous catalysts [8,32–34].

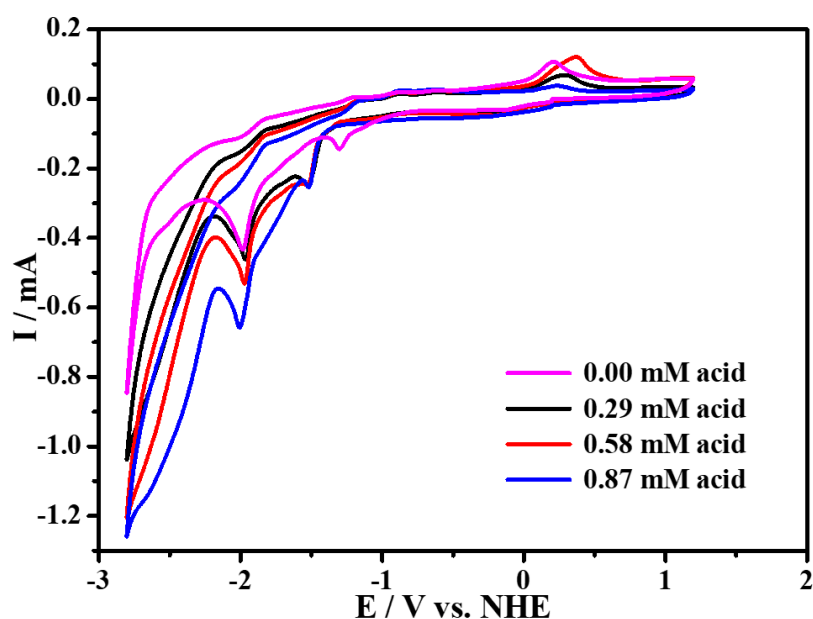


Figure 7. Cyclic voltammograms of complex **1** (2 mM) recorded in the absence (rose red trace) and in the presence of TsOH·H₂O: 1 equiv (black trace), 2 equiv (red trace), and 3 equiv (blue trace) in CH₃CN (0.1 M ⁿBu₄NPF₆) at a glassy carbon electrode and 100 mV s⁻¹.

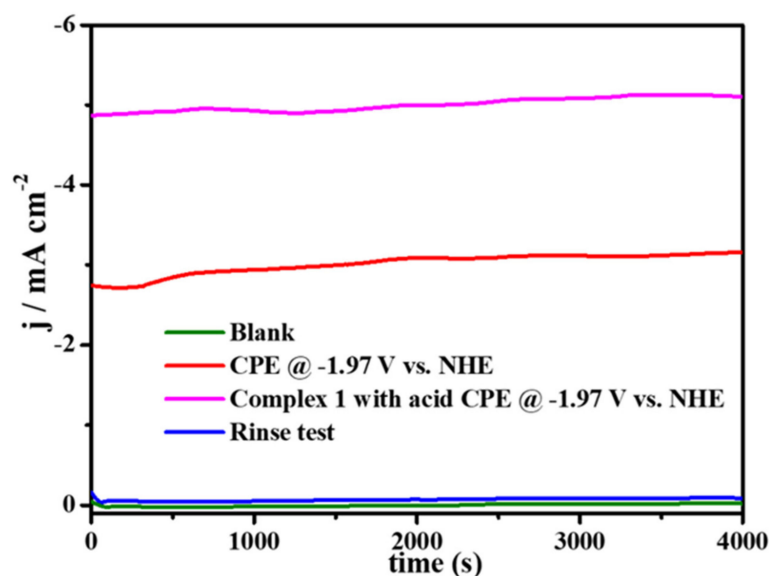


Figure 8. CPE of 2 mM complex **1** in CH₃CN (0.1 M ⁿBu₄NPF₆) (red) or in CH₃CN (0.1 M ⁿBu₄NPF₆) (rose red) solutions with 0.58 mM TsOH·H₂O added; no complex **1** (green) under an atmosphere of Ar on the FTO working electrode; rinse test (blue).

Moreover, the rinse test conducted on the FTO glass electrode after electrocatalysis shows almost no current density, which resembles that of the blank test before the catalysis (Figure 8), revealing that complex **1** can homogeneously catalyze H⁺ reduction with high stability. The DLS of complex **1** proved that no nanoparticles were formed before and after electrolysis for 4000 s, indicating that it has excellent stability, as illuminated in Figure S15a (Supplementary Materials). Additionally, the nearly linear curve of CPE indicates that catalyst **1** can remain stable in solution throughout the catalytic process. Furthermore, as shown in Figure S12 (Supplementary Materials), during CPE for 4000 s, the in-situ UV-vis spectroelectrochemistry of complex **1** displays negligible difference in the spectrum, confirming the great stability of catalyst **1** during electrolysis.

3. Materials and Methods

3.1. Synthesis

The ligand $L^1 = 2-(6\text{-methoxypyridin-2-yl})\text{-6-nitro-1h-benzo [D] imidazole}$ was synthesized according to the previous report [35]. $\text{Cu}(\text{NO}_3)_2 \cdot 3\text{H}_2\text{O}$ (0.242 g, 1 mmol) was added to 15 mL acetonitrile solution of L^1 (0.782 g, 2 mmol), and stirred at room temperature for 12 h. The resulting solution was filtered, and the filtrate was kept for evaporation at room temperature for about 7 days to give X-ray-quality dark green crystals. Yield: 0.384 g (57.9%). Calc. (Found) for $\text{C}_{26}\text{H}_{18}\text{CuN}_{10}\text{O}_{12}$: C, 48.75(48.62); H, 2.81(2.99); N, 19.69(19.54). IR (KBr disk, cm^{-1}): 3092 (m), 1591 (m), 1471 (m), 1422 (m), 1319 (s), 1047 (w), 803 (w), 732(w), and 607(w) (Figure S1, Supplementary Materials). The purity of the synthesized complex **1** was confirmed by powder X-ray diffraction (PXRD) analysis, which shows that the peak positions of the diffraction in their experimental and theoretical PXRD patterns all agreed well (Figure S4, Supplementary Materials), demonstrating that the prepared samples are all pure.

3.2. General Materials and Characterization

The solvents and materials used are reagent grade and have not been purified. Unless otherwise stated, all the operations are carried out under aerobic conditions, all the chemicals are commercially available and can be used without further purification, and the carbon dioxide and argon are purchased from Dehai Gas Company (Hainan, China). X-ray powder diffraction (XRD) (Figure S4) is carried out on the Bruker D8 powder diffraction instrument in order to obtain the purity of the complement and the sample of the complex. After complex fracks with pure KBr, infrared spectral data (Figure S1, Supplementary Materials) is recorded by the Nicolet 170SX infrared spectrometer (Thermo Fisher, Waltham, MA, USA) in the $4000\text{--}500\text{ cm}^{-1}$ scanning range. Elemental analysis uses 2400 PerkinElmer analyzers to examine the percentage content of C, H, and N elements of the mates, and the theoretical values are basically consistent.

3.3. Crystal Structure Determination

The structural data of crystal is collected using the Bruker Smart-1000 CCD X-ray monocrystalline diffraction instrument (Bruker, Germany), all of which is restored by the SAINT v8.34A program (Bruker, 2013) and corrected and absorbed using the SADABS program (Bruker, 2014/5). The SHELXL software (v.2014/7, Software Fayre, Madrid, Spain) and Olex2 software (v.1.2, OlexSys Ltd., Durham, England) parse the initial structure by direct method, refining it with F^2 -based full matrix least square technology [36,37], and this technique is used to modify the non-O atomic coordinates and anisotropy. Table S1 (Supplementary Materials) gives cell parameters, spatial groups, some conventional thermodynamic parameters, and other data of the crystal, and it introduces the relevant crystal information in detail. Tables S2 and S3 (Supplementary Materials) list the selected key length and key angles. The anion of the molecule is severely disordered, thus a Platon-Squeeze [38] was used to refine the anion-free structure of complex **1**.

3.4. Electrochemical Measurement and Electrolytic Product Analysis

All electrochemical experiments are tested with CHI660E electrochemical analyzers in order to study their electrocatalytic properties, and these experiments are conducted in single-chamber three-electrode reactors. A solution of 0.1 M $n\text{Bu}_4\text{NPF}_6$ in a dry acetonitrile was used as the supporting electrolyte. Cyclic voltammogram (CV) experiments were carried out using a glass carbon working electrode with a diameter of 3 mm, which was carefully polished with diamond plaster, and ultrasonically cleaned in aqueous ethanol and deionized water, and then dried before use.

There is close to 20 mL of solution in the electrolytic cell, and the concentration of the complex in the solution is close to 0.1 mol/L. The anti-electrode is platinum wire, and the reference electrode is the Ag/AgCl electrode. A conductive glass substrate doped with fluorine tin oxide (FTO) ($1\text{ cm} \times 1\text{ cm}$, effective surface area of 1.0 cm^2) (produced by

Zhuhai Kaivo Optoelectronic Corp., Zhuhai, China) is used as an operating electrode to control potential electrolysis (CPE), which is soaked with 5 wt% NaOH in ethanol solution for several hours, and then washed with water, ethanol, and water in turn. Before each experiment, the solution is blown away at room temperature with Ar or CO₂ for 30 min. CPE at the same condition on GCE is shown in Figure S6 (Supplementary Materials).

In-situ UV-visible spectral electrochemistry is performed by applying the constant potentials of -1.15 V (Figure S8, Supplementary Materials) and -1.97 V vs. NHE (Figure S12, Supplementary Materials) under CO₂ and Ar atmosphere, respectively, and recorded using the UV-visible spectrophotometer (Shimadzu, Kyoto, Japan). In-situ spectral electrochemistry studies use quartz dishes with a path length of 1 cm as electrochemical batteries, including platinum mesh, platinum wire, and Ag/AgCl (saturated KCl) electrodes, respectively, as working electrodes, anti-electrodes, and reference electrodes. The top space gas sample (2 mL) produced by the capillary tube electrophoresis experiment is extracted using a bait-locked airtight syringe and injected into the gas chromatography (GC, Shimadzu GC-2014), equipped with a flame ionization detector (FID) containing a mechanical device to analyze carbon monoxide, and equipped with a thermal conductivity detector (TCD, Shimadzu) for analysis to quantify H₂. Detection of CO₂ and H₂ are carried out with ultra-high purity Ar as carrier gas. Liquid products are analyzed by NMR (Bruker AVANCE III HD).

3.5. Density Functional Theory Calculations

Quantum-mechanical calculations were carried out utilizing the Gaussian 09 program package, using the B3LYP hybrid functional [39,40]; the “double- ξ ” quality LanL2DZ [41] basis sets were used for transition metals (Cu), and 6-311G (d, p) basis sets were used for non-metal atoms [42]. The atom coordinates used in the calculations were gained from crystallographic data, and a molecule in the unit cells was selected as the initial model.

4. Conclusions

In this work, we have successfully synthesized a novel copper (II) electrocatalyst [Cu(L¹)₂NO₃]₂NO₃ (**1**) containing the redox active ligand 2-(6-methyl-2-base)-6-nitro-1H-benzene and [d] imidazole (L¹). Through investigation, we discovered that complex **1** can electrocatalyze CO₂ reduction to CO and HER. While adding water as the proton source in the system for CO₂ reduction, the reactivity for CO₂ reduction of complex **1** is enhanced. However, due to the competitive reaction of H⁺ reduction, the mixed gas CO and H₂ are both evolved with the FE of 10% and 90%, respectively. Resultingly, we additionally studied its catalytic activity for HER, and observed that, with the increasing amounts of p-Toluenesulfonic acid added in the solution, the electrocatalytic reactivity for HER increased. Furthermore, in-situ UV-vis spectroelectrochemistry of complex **1** during CO₂ reduction and HER were both carried out, and these both displayed negligible difference in the spectrum, confirming the great stability of catalyst **1** during electrolysis. Combined with DFT calculation, it has been confirmed that the great electrocatalytic performance of complex **1** is owing to the synergistic effect between the metal center Cu (II) and the redox-active ligand L¹.

Supplementary Materials: Table S1. Crystallographic data for the complex **1**. Table S2. The main key length of the complex **1**. Table S3. The main key angle of the complex **1**. Table S4. Cartesian coordinates for **1**. Figure S1. IR spectrum of the complex **1**. Figure S2. HOMO-LUMO orbitals of complex **1**. Figure S3. (a) LUMO+1 orbital; (b) LUMO+2 orbital; (c) HOMO-1 orbital; and (d) HOMO-2 orbital. Figure S4. Powder X-ray diffraction (PXRD) patterns of complex **1**. Figure S5. Cyclic voltammetry of 2 mM ligand L¹ under 1 atm Ar at scan rate 100 mV s⁻¹. Table S5. The reduction potentials and peak currents of complex **1** under 1 atm Ar in a 0.1 M ⁿBu₄NPF₆ CH₃CN supporting electrolyte. Table S6. The reduction potentials and peak currents of complex **1** under 1 atm CO₂ (in addition to Ar) in a 0.1 M ⁿBu₄NPF₆ CH₃CN supporting electrolyte. Table S7. The reduction potentials and peak currents of complex **1** containing different concentrations of H₂O under CO₂ (in addition to base line). Table S8. The reduction potentials and peak currents of complex **1** with

different concentrations under 1 atm CO₂ (in addition to base line) in a 0.1 M ⁿBu₄NPF₆ CH₃CN supporting electrolyte. Figure S6. (a) CPE for H₂ evolution (black line) at −1.97 V vs NHE on GCE (0.07 cm²); (b) CPE for CO₂ reduction (red line) at −1.15 V vs NHE on GCE (0.07 cm²) at the same condition as using FTO. Figure S7. CPE with 2 mM complex 1 (rose red line), rinse test (green line) and the blank experiment without 1 (blue line) on an FTO working electrode (1.0 cm²). Figure S8. The in-situ UV-Vis spectroelectrochemistry of complex 1 in CO₂ atmosphere. Figure S9: (a) the amount of material in the proton supply system that is combined with the electrocatalytic reduction CO₂ product; and (b) the Faraday efficiency curves of the electrocatalytic reduction products CO and H₂ in the proton supply H₂O system. Figure S10. Cyclic voltammetry of complex 1 in the presence (green) and absence (black) of CO₂ recorded at 100 mV s^{−1} at glassy carbon in a 0.1 M ⁿBu₄NPF₆ CH₃CN supporting electrolyte. Figure S11. Cyclic voltammograms of complex 1 (2 mM) recorded in the presence of 0.58 mM TsOH·H₂O under 1 atm Ar at scan rate range from 100 to 500 mV s^{−1} in CH₃CN (0.1 M ⁿBu₄NPF₆) at a glassy carbon electrode. Figure S12. The in-situ UV-Vis spectroelectrochemistry of complex 1 in Ar atmosphere. Figure S13. Cyclic voltammograms of complex 1 (2 mM, red trace) and in the presence of 10 mM TsOH·H₂O (black trace) in CH₃CN (0.1 M ⁿBu₄NPF₆) at a glassy carbon electrode and 100 mV s^{−1}. Figure S14. Cyclic voltammograms recorded in the absence (black trace) or in the presence of 10 mM of TsOH·H₂O (red trace). Scan rate: 100 mV s^{−1}. Working electrode: glassy carbon. Counter electrode: Pt wire. Reference electrode: Ag/AgCl. Figure S15. DLS spectra of the electrolyte before and after the CPE test: (a) DLS of the complex 1 containing 0.58mM TsOH·H₂O in CH₃CN (0.1 M ⁿBu₄NPF₆) before and after 4000 s electrolysis; and (b) DLS of the complex 1 in CH₃CN (0.1 M ⁿBu₄NPF₆) under 1 atm CO₂ before and after 4000 s electrolysis. Figure S16. The Faraday efficiency curves of the electrocatalytic hydrogen evolution products H₂ in the proton supply 0.58 mM TsOH·H₂O system. Figure S17. Plot of the magnetic moments (μ_{eff}) versus the temperature T for solid sample of complex 1. Table S9. The molecular geometries of complex 1 as predicted by SHAPE.

Author Contributions: Conceptualization, J.L., J.W., X.Y. and Z.H.; Data curation, J.L.; Formal analysis, J.L.; Funding acquisition, M.W.; Investigation, J.L., G.C., D.Z. and M.W.; Methodology, J.L. and J.W.; Project administration, M.W.; Resources, S.Z.; supervision, G.C., D.Z. and M.W.; Writing—original draft, J.L.; Writing—review and editing, J.L. and M.W. All authors have read and agreed to the published version of the manuscript.

Funding: This research was funded by Russian Science Foundation, grant No. 19-13-00016.

Institutional Review Board Statement: Not applicable.

Informed Consent Statement: Informed consent was obtained from all subjects involved in the study. Written informed consent has been obtained from the patient(s) to publish this paper.

Data Availability Statement: The data presented in this study are available on request from the corresponding author. The data are not publicly available due to this being part of federally funded research.

Acknowledgments: This work has been funded by the National Natural Science Foundation of China (No. 21601171), the Shandong Natural Science Foundation (No. ZR2016BB08), and the Central University Foundation for Basic Research (No. 201713028).

Conflicts of Interest: The authors declare no conflict of interest.

Sample Availability: Samples of the compounds are available from the authors.

References

1. Gurney, K.R.; Mendoza, D.L.; Zhou, Y.; Fischer, M.L.; Miller, C.C.; Geethakumar, S.; de la Rue du Can, S. High resolution fossil Fuel Combustion CO₂ emission fluxes for combustion the united states. *Environ. Sci. Technol.* **2009**, *43*, 5535–5541. [[CrossRef](#)]
2. Peng, Y.; Wu, T.; Sun, L.; Nsanjimana, J.M.V.; Fisher, A.C.; Wang, X. Selective electrochemical reduction of CO₂ to ethylene on Nanopores-Modified copper electrodes in aqueous solution. *ACS Appl. Mater. Inter.* **2017**, *9*, 32782–32789. [[CrossRef](#)] [[PubMed](#)]
3. Wang, T.; Xie, H.; Chen, M.; D’Aloia, A.; Cho, J.; Wu, G.; Li, Q. Precious metal-free approach to hydrogen electrocatalysis for energy conversion: From mechanism understanding to catalyst design. *Nano Energy* **2017**, *42*, 69–89. [[CrossRef](#)]
4. Anantharaj, S.; Kundu, S. Do the evaluation parameters reflect intrinsic activity of electrocatalysts in electrochemical water splitting? *ACS Energy Lett.* **2019**, *4*, 1260–1264. [[CrossRef](#)]

5. Yang, C.; Wang, Y.; Qian, L.; Al-Enizi, A.M.; Zhang, L.; Zheng, G. Heterogeneous electrocatalysts for CO₂ reduction. *ACS Appl. Energy Mater.* **2021**, *4*, 1034–1044. [[CrossRef](#)]
6. Xiong, B.; Yang, Y.; Liu, J.; Ding, J.; Yang, Y. Electrochemical conversion of CO₂ to syngas over Cu-M (M = Cd, Zn, Ni, Ag, and Pd) bimetal catalysts. *Fuel* **2021**, *304*, 121341. [[CrossRef](#)]
7. Zhang, L.; Li, X.; Lang, Z.; Liu, Y.; Liu, J.; Yuan, L.; Lu, W.; Xia, Y.; Dong, L.; Yuan, D.; et al. Enhanced cuprophilic interactions in crystalline catalysts facilitate the highly selective electroreduction of CO₂ to CH₄. *J. Am. Chem. Soc.* **2021**, *143*, 3808–3816. [[CrossRef](#)]
8. Drosou, M.; Kamatsos, F.; Ioannidis, G.; Zarkadoulas, A.; Mitsopoulou, C.A.; Papatriantafyllopoulou, C.; Tzeli, D. Reactivity and mechanism of photo- and electrocatalytic hydrogen evolution by a diimine Copper(I) complex. *Catalysts* **2020**, *10*, 1302. [[CrossRef](#)]
9. Liu, D.; Ke, M.; Ru, T.; Ning, Y.; Chen, F. Room-temperature Pd-catalyzed methoxycarbonylation of terminal alkynes with high branched selectivity enabled by bisphosphine-picolinamide ligand. *Chem. Commun.* **2017**, *27*, 9359–9363. [[CrossRef](#)]
10. Queyriaux, N. Redox-Active ligands in electroassisted catalytic H⁺ and CO₂ reductions: Benefits and risks. *ACS Catal.* **2021**, *11*, 4024–4035. [[CrossRef](#)]
11. Lyaskovskyy, V.; de Bruin, B. Redox Non-Innocent ligands: Versatile new tools to control catalytic reactions. *ACS Catal.* **2012**, *2*, 270–279. [[CrossRef](#)]
12. Wang, M.; England, J.; Weyhermüller, T.; Kokatam, S.; Pollock, C.J.; Debeer, S.; Shen, J.; Yap, G.P.A.; Theopold, K.H.; Wieghardt, K. New complexes of Chromium (III) containing organic π -Radical ligands: An experimental and density functional theory study. *Inorg. Chem.* **2013**, *52*, 4472–4487. [[CrossRef](#)]
13. Natesakhawat, S.; Lekse, J.W.; Baltrus, J.P.; Ohodnicki, P.R.; Howard, B.H.; Deng, X.; Matranga, C. Active sites and structure–activity relationships of Copper-Based catalysts for carbon dioxide hydrogenation to methanol. *ACS Catal.* **2012**, *2*, 1667–1676. [[CrossRef](#)]
14. Su, X.; Mccardle, K.M.; Chen, L.; Panetier, J.A.; Jurss, J.W. Robust and selective cobalt catalysts bearing Redox-Active Bipyridyl-N-heterocyclic carbene frameworks for electrochemical CO₂ reduction in aqueous solutions. *ACS Catal.* **2019**, *9*, 7398–7408. [[CrossRef](#)]
15. Shi, N.N.; Xie, W.J.; Gao, W.S.; Wang, J.M.; Zhang, S.F.; Fan, Y.H.; Wang, M. Effect of PDI ligand binding pattern on the electrocatalytic activity of two Ru (II) complexes for CO₂ reduction. *Appl. Organomet. Chem.* **2020**, *34*, e5551. [[CrossRef](#)]
16. Tok, G.C.; Reiter, S.; Freiberg, A.T.S.; Reinschlüssel, L.; Gasteiger, H.A.; de Vivie-Riedle, R.; Hess, C.R. H₂ Evolution from Electrocatalysts with Redox-Active Ligands: Mechanistic Insights from Theory and Experiment vis-à-vis Co-Mabiq. *Inorg. Chem.* **2021**, *60*, 13888–13902. [[CrossRef](#)]
17. Orchanian, N.M.; Hong, L.E.; Velazquez, D.A.; Marinescu, S.C. Electrocatalytic syngas generation with a redox non-innocent cobalt 2-phosphinobenzenethiolate complex. *Dalton Trans. Int. J. Inorg. Chem.* **2021**, *50*, 10779–10788. [[CrossRef](#)]
18. Zhang, W.; Huang, C.; Zhu, J.; Zhou, Q.; Yu, R.; Wang, Y.; An, P.; Zhang, J.; Qiu, M.; Zhou, L.; et al. Dynamic restructuring of coordinatively unsaturated copper paddle wheel clusters to boost electrochemical CO₂ reduction to hydrocarbons**. *Angew. Chem. Int. Ed.* **2021**, *61*, e5551.
19. Jiang, Y.; Deng, Y.; Liang, R.; Fu, J.; Gao, R.; Luo, D.; Bai, Z.; Hu, Y.; Yu, A.; Chen, Z. D-Orbital steered active sites through ligand editing on heterometal imidazole frameworks for rechargeable zinc-air battery. *Nat. Commun.* **2020**, *11*, 5858. [[CrossRef](#)]
20. Ghosh, P.; Vos, S.; Lutz, M.; Gloaguen, F.; Schollhammer, P.; Moret, M.E.; Klein Gebbink, R.J.M. Electrocatalytic proton reduction by a cobalt complex containing a proton-responsive bis(alkylimidazole)methane ligand: Involvement of a C–H bond in H₂ formation. *Chem. Eur. J.* **2020**, *26*, 12560–12569. [[CrossRef](#)]
21. Thorp, W.L.A.H. Bond valence sum analysis of Metal-Ligand bond lengths in metalloenzymes and model. *Inorg. Chem.* **1993**, *19*, 4102–4105. [[CrossRef](#)]
22. Bersuker, I.B. Pseudo-Jahn–Teller effect—A Two-State paradigm in formation, deformation, and transformation of molecular systems and solids. *Chem. Rev.* **2013**, *113*, 1351–1390. [[CrossRef](#)] [[PubMed](#)]
23. Alvarez, S.; Avnir, D.; Llunell, M.; Pinsky, M. Continuous symmetry maps and shape classification. The case of six-coordinated metal compounds. Electronic supplementary information (ESI) available: Tables of CSD refcodes, structural parameters and symmetry measures for the studied compounds. *New J. Chem.* **2002**, *26*, 996–1009. [[CrossRef](#)]
24. Pinsky, M.; Avnir, D. Continuous Symmetry Measures. 5. The Classical Polyhedra. *Inorg. Chem.* **1998**, *37*, 5575–5582. [[CrossRef](#)]
25. Pandey, S.; Kumar, G.; Gupta, R. Postfunctionalized Metalloligand-Based catenated coordination polymers: Syntheses, structures, and effect of labile sites on catalysis. *Cryst. Growth Des.* **2019**, *19*, 2723–2735. [[CrossRef](#)]
26. Schlagintweit, J.F.; Dyckhoff, F.; Nguyen, L.; Jakob, C.H.G.; Reich, R.M.; Kühn, F.E. Mixed tetradentate NHC/1,2,3-triazole iron complexes bearing cis labile coordination sites as highly active catalysts in Lewis and Brønsted acid mediated olefin epoxidation. *J. Catal.* **2020**, *383*, 144–152. [[CrossRef](#)]
27. Biswas, S.; Chowdhury, S.N.; Lepcha, P.; Biswas, A.N. Pentadentate Copper (II)-amidate complex as a precatalyst for electrocatalytic proton reduction. *Int. J. Hydrog. Energ.* **2021**, *46*, 21542–21548. [[CrossRef](#)]
28. Xiao, Y.; Zhang, Y.; Zhai, R.; Gu, Z.; Zhang, J. Helical copper-porphyrinic framework nanoarrays for highly efficient CO₂ electroreduction. *Sci. China Mater.* **2021**, 1–7. [[CrossRef](#)]

29. Lu, Y.F.; Dong, L.Z.; Liu, J.; Yang, R.X.; Liu, J.J.; Zhang, Y.; Zhang, L.; Wang, Y.R.; Li, S.L.; Lan, Y.Q. Predesign of catalytically active sites via stable coordination cluster model system for electroreduction of CO₂ to ethylene. *Angew. Chem. Int. Ed.* **2021**, *60*, 26210–26217. [[CrossRef](#)]
30. Li, G.; Zhao, Y.; Li, J.P.H.; Chen, W.; Li, S.; Dong, X.; Song, Y.; Yang, Y.; Wei, W.; Sun, Y. Insight into Composition and Intermediate Evolutions of Copper-Based Catalysts during Gas-Phase CO₂ Electroreduction to Multicarbon Oxygenates. *Catalysts* **2021**, *11*, 1502. [[CrossRef](#)]
31. Wei, L.; Ye, B. Efficient Conversion of CO₂ via Grafting Urea Group into a [Cu₂(COO)₄]-Based Metal–Organic Framework with Hierarchical Porosity. *Inorg. Chem.* **2019**, *58*, 4385–4393. [[CrossRef](#)]
32. Zhang, Y.; Cao, Q.; Wu, X.; Xiao, Y.; Meng, A.; Zhang, Q.; Yu, Y.; Zhang, W. Efficient photocatalytic H₂ evolution and α-methylation of ketones from copper complex modified polymeric carbon nitride. *Chem. Eng. J.* **2022**, *427*, 132042. [[CrossRef](#)]
33. Datta, A.; Das, K.; Beyene, B.B.; Garribba, E.; Gajewska, M.J.; Hung, C. EPR interpretation and electrocatalytic H₂ evolution study of bis(3,5-di-methylpyrazol-1-yl) acetate anchored Cu (II) and Mn (II) complexes. *Mol. Catal.* **2017**, *439*, 81–90. [[CrossRef](#)]
34. Lei, H.; Fang, H.; Han, Y.; Lai, W.; Fu, X.; Cao, R. Reactivity and mechanism studies of hydrogen evolution catalyzed by copper corroles. *ACS Catal.* **2015**, *5*, 5145–5153. [[CrossRef](#)]
35. Chen, S.; Fan, R.; Wang, X.; Yang, Y. Novel bright blue emissions IIB group complexes constructed with various polyhedron-induced 2-[2'-(6-methoxy-pyridyl)]-benzimidazole derivatives. *Crystengcomm* **2014**, *16*, 6114. [[CrossRef](#)]
36. Sheldrick, G.M. Crystal structure refinement with SHELXL. *Acta Crystallogr. Sect. C* **2015**, *71*, 3–8. [[CrossRef](#)]
37. Dolomanov, O.V.; Bourhis, L.J.; Gildea, R.J.; Howard, J.A.; Puschmann, H. OLEX2: A complete structure solution, refinement and analysis program. *J. Appl. Crystallogr.* **2009**, *42*, 339–341. [[CrossRef](#)]
38. Spek, A.L. Structure validation in chemical crystallography. *Acta Crystallogr. Sect. D Biol. Crystallogr.* **2009**, *65*, 148–155. [[CrossRef](#)] [[PubMed](#)]
39. Becke, A.D. Density-functional thermochemistry. III. The role of exact exchange. *J. Chem. Phys.* **1993**, *98*, 5648–5652. [[CrossRef](#)]
40. Lee, C.; Yang, W.; Parr, R.G. Development of the Colic-Salvetti correlation-energy into a functional of the electron density. *Phys. Rev. B* **1988**, *37*, 785. [[CrossRef](#)] [[PubMed](#)]
41. Hay, P.J.; Wadt, W.R. Ab initio effective core potentials for molecular calculations. Potentials for K to Au including the outermost core orbitals. *J. Chem. Phys.* **1985**, *82*, 299–310. [[CrossRef](#)]
42. Cometto, C.; Chen, L.; Lo, P.; Guo, Z.; Lau, K.; Anxolabéhère-Mallart, E.; Fave, C.; Lau, T.; Robert, M. Highly selective molecular catalysts for the CO₂-to-CO electrochemical conversion at very low overpotential. Contrasting Fe vs Co quaterpyridine complexes upon mechanistic studies. *ACS Catal.* **2018**, *8*, 3411–3417. [[CrossRef](#)]